

LIGO SURF Final Report

Improved Targeted sub-threshold Search for Strongly Lensed Gravitational Waves with Sky Location Constraint

Aidan H.Y. Chong,^{1, a}

Mentors: Alvin Li,^{2, b} Ryan Magee,^{2, c} Juno C.L. Chan,^{1, d} Cody Messick,^{3, e} and Alan J. Weinstein^{2, f}

¹*Department of Physics, The Chinese University of Hong Kong*

²*LIGO Laboratory, California Institute of Technology*

³*LIGO Laboratory, Massachusetts Institute of Technology*

(Dated: April 2022)

Gravitational lensing is an important field in both astrophysics and cosmology as it could provide a large amount of crucial information about our universe unmatched by other phenomena, such as the determination of the expansion rate of the universe and the distribution of dark matter. Until recently, gravitational lensing was only applied to observing the electromagnetic spectrum. Since the first successful observation of gravitational waves back in 2015, discussions have started to try to find lensed gravitational wave signals. However, in most cases, the lensed image should be much dimmer than the original signal, which might be buried in the noise as it could not pass the normal detection threshold. Our work would be to improve the existing TESLA searching pipeline to suit our lensing search needs. We hope to recover the originally buried sub-threshold lensed signal from the collected data. Our work would be implemented in the TESLA pipeline for future uses.

I. INTRODUCTION

Gravitational waves, predicted by Albert Einstein's theory of General Relativity proposed in 1915 [1], were first detected by LIGO (Laser Interferometer Gravitational-Waves Observatory) in 2015 [2]. Since then, more than 90 gravitational waves from compact binary coalescences have been detected in the three observing runs [3–6]. Gravitational waves open a new window for us to study the universe, which allows us to fine-tune the modelling of neutron stars [7–9], understand the formation channels of astrophysical objects [7, 10], study the early universe using the stochastic background [11, 12] and find out the expansion rate of the universe by measuring the Hubble's parameter [13, 14].

General relativity dictates that massive objects can curve spacetime, and hence when light passes by massive objects, its path will be refracted and deflected before reaching the observer while being magnified or demagnified, hence forming multiple images arriving at different times. Such a phenomenon is known as gravitational lensing. Gravitational lensing is widely applied in astrophysics and cosmology. A gravitational lens can give information on the image source, the object acting as the lens, and notably the intervening large-scale geometry of the universe in which the source, object, and the observer are at cosmological distances from each other [15]. From the equivalence principle, gravitational waves should be lensed similarly. Since the first detection of gravitational waves, many efforts have been made to claim,

and denial of observing lensed gravitational waves have been made [16–18]. To this date, there is not enough compelling evidence to show lensed pairs in the catalogue of confirmed gravitational wave events [19].

Due to the sheer amount of data collected in multiple observing runs, we could not analyse all of the data collected at every instance as it would be too computationally costly. Instead, we only choose to analyse signals that pass certain detection thresholds. The thresholds are usually intensity, which measures how intense the collected signal is. In other words, a signal with a signal-to-noise ratio (SNR) greater than a certain threshold value would produce a trigger. We would then perform analyses on the triggers utilising statistical parameters such as likelihood ratio to determine how likely it would be a true gravitational wave signal. Currently available pipelines for such searching of triggers includes GstLAL [20], MBTA [21], SPIIR [22] and PyCBC [23]. However, it is easy to see that some real gravitational wave signals with relatively low intensities, either due to the source being too far from Earth or demagnified by gravitational lensing, would be discarded as noise without producing a trigger. These low-intensity signals are called sub-threshold signals. Recovering these sub-threshold signals is important for lensing searches as we expect different lensed images will have different intensities, and some would be in the sub-threshold category.

While lensed images have different sky locations, the deviation (of the order of arc-seconds) is much smaller than the accuracy of the sky location inferred for sources of gravitational waves (in order of degrees). Hence we can treat lensed gravitational waves as if they are coming from the same sky location. In this research, we aim to further improve the sensitivity of the targeted search for sub-threshold lensed gravitational waves by including the extra constraint that they have to come from the same sky location as the target, which

^a 1155160056@link.cuhk.edu.hk

^b kli7@caltech.edu

^c ry.m.magee@gmail.com

^d clchan@phy.cuhk.edu.hk

^e cmessick@mit.edu

^f ajw@caltech.edu

is lacking in the current searches.

This paper is structured as follows. Section II presents the important background knowledge related to our research. Section III provides the method used in this research. Section IV outlines the procedure used during this project. Lastly, section V would be the future plans after completing this LIGO SURF project.

II. BACKGROUND

A. Physics of Gravitational Waves

Einstein's theory of General Relativity treated time as a spatial dimension, so together with 3D space, they constitute 4D space-time. Einstein's field Equation is the equation responsible for giving the relationship between the motion of masses and the curvature of space-time. Mathematically speaking, the equation is written as¹

$$R_{\mu\nu} - \frac{1}{2}Rg_{\mu\nu} = 8\pi T_{\mu\nu}, \quad (1)$$

where $R_{\mu\nu}$ is the Ricci tensor, R is Ricci scalar, $g_{\mu\nu}$ is the metric tensor, and $T_{\mu\nu}$ is the Energy-Momentum tensor. From the equation, we can easily observe that the left-hand side represents the curvature of space-time and the right-hand side represents the energy and momentum of the object. As a result, mass in space-time would affect the curvature of the space-time around it.

From Einstein's field Equation, we can see that masses can warp spacetime. When a nonspherical and nonuniform mass is in motion, it produces ripples of curved spacetime. [15]. According to special relativity, the speed of causality is equal to the speed of light c [24], which means no signal could be transmitted faster than the speed of light, not even gravity. In this case, general relativity predicts that the speed of gravity, which also includes the propagating speed of gravitational waves, would be travelling at the speed of light. Multi-messenger observation of GW170817 binary neutron star event has constrained the difference between the speed of gravity and the speed of light to be between -3×10^{-15} and $+7 \times 10^{-16}$ times the speed of light [7, 25], which is very close to the theoretical value. There are many sources of gravitational waves in our universe, including compact binary coalescence (CBC), supernova explosions, and the big bang [15]. Sadly, to this date, we have only confirmed to detect gravitational waves from CBC. For that reason, this research would only focus on gravitational waves emitted by CBC.

The curvature of space-time is embedded in the metric tensor. For a flat space-time without curvature (Minkowski spacetime), the metric of flat spacetime is given by

$$g_{\alpha\beta}(x) = \eta_{\alpha\beta}, \quad (2)$$

where g is the metric and

$$\eta_{\alpha\beta} = \begin{bmatrix} -1 & 0 & 0 & 0 \\ 0 & 1 & 0 & 0 \\ 0 & 0 & 1 & 0 \\ 0 & 0 & 0 & 1 \end{bmatrix}. \quad (3)$$

When a small amplitude gravitational plane wave propagates through the cosmos towards Earth, the space-time where the wave travels through can be approximated to be a flat space-time (Minkowski space-time) with very high accuracy [15]. We consider adding a small perturbation term $h_{\alpha\beta}$ to flat spacetime (with $|h_{\alpha\beta}| = 1$), such that the metric now becomes

$$g_{\alpha\beta}(x) = \eta_{\alpha\beta} + h_{\alpha\beta}(x), \quad (4)$$

where $h_{\alpha\beta}(x)$ is the small perturbations to the flat space-time metric, and we expand Einstein's field equation to the linear order of $h_{\alpha\beta}$, we will arrive at

$$\square^2 h_{\alpha\beta} = -16\pi T_{\alpha\beta}. \quad (5)$$

For the region outside the source of gravitational waves, it is approximately a vacuum. Therefore, $T_{\alpha\beta} = 0$ in the space outside the source. Hence we have

$$\square^2 h_{\alpha\beta} = 0, \quad (6)$$

which allows a plane-wave solution.

In the traceless-transverse (TT) gauge, the perturbation term of a gravitational wave travelling in the z -direction can be written as

$$h_{\alpha\beta}^{\text{TT}}(t, z) = \begin{bmatrix} 0 & 0 & 0 & 0 \\ 0 & h_+ & h_\times & 0 \\ 0 & h_\times & -h_+ & 0 \\ 0 & 0 & 0 & 0 \end{bmatrix} \cos(t - z), \quad (7)$$

Where h_+ and h_\times are the plus and cross-polarization content respectively. When the gravitational wave passes through a ring of test masses placed on the $x - y$ plane, it deforms the ring of test masses according to the polarization of the wave, as shown figure 1.

B. Detection of Gravitational Waves

Currently, all the detected gravitational waves were produced by the merger of massive and dense bodies such as black holes and neutron stars. Space-time will be heavily distorted when the two bodies clash, and the weak field approximation breaks down. Numerical simulations must be

¹ Units of $c = G = 1$ would be used throughout the report

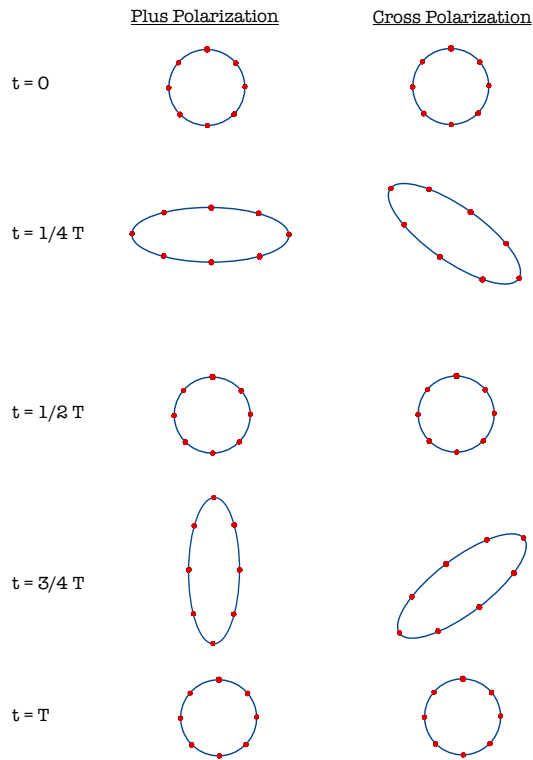


Figure 1. The behaviour of test masses under the influence of gravitational waves of different polarization. The period is T , and t is the time since the beginning of the period. When a plus polarized gravitational wave propagates through spacetime, the test masses stretch in 2 perpendicular direction that together looks like a "+" shape, while for cross polarisation, it looks like a "×" shape.

employed to find out the waveform in those situations.

The typical waveform of gravitational waves could be classified into three stages. The positions of the three stages were illustrated in figure 2. The inspiral and Ringdown stages could use perturbation theories to find approximated solutions, but the merger stage could only be calculated using numerical simulation.

The LIGO-Virgo-KAGRA (LVK) collaboration has four detectors altogether in Hanford, Livingston, Europe, and Japan. At the time of writing, VIRGO in Europe and KARGA in japan are already operating. The detectors are Michaelson interferometers [26] with similar working principles to the LIGO detectors with minor differences in their designs. Figure 3 shows the schematic diagram of a LVK gravitational-wave detector. The entire setup is placed inside a vacuum to reduce the thermal noise caused by the Brownian motion of air molecules and to reduce the probability of dust molecules blocking the path of light or sticking to the mirrors themselves [27], which would hinder the accuracy of the detector. The arm length L is set to be 4km long. The reason for constructing such a long arm is to elevate the sensitivity of the detector [28], although an effective distance of 4km is

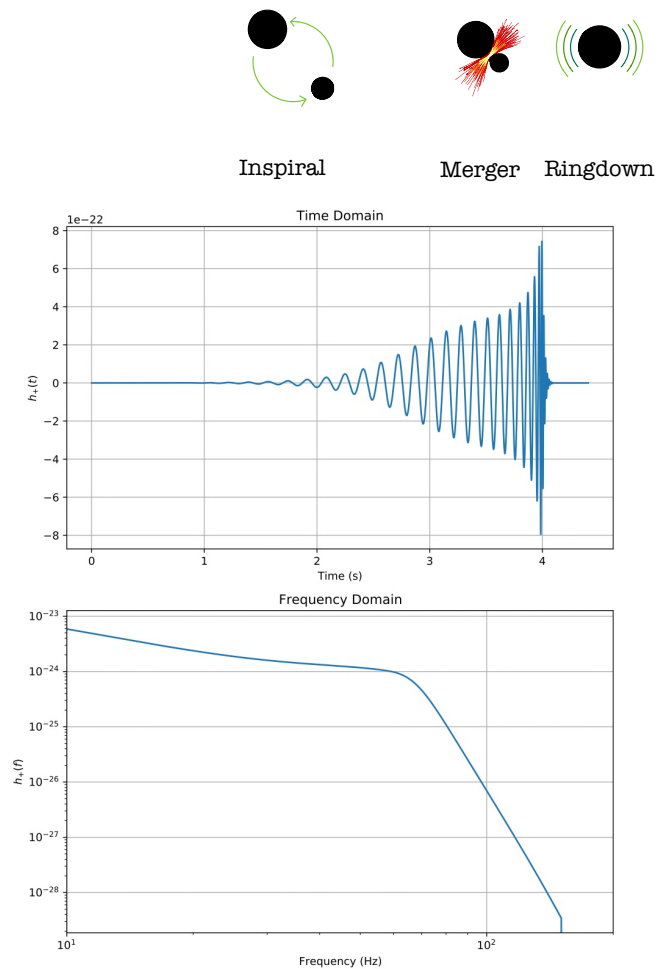


Figure 2. Top: Illustrations of the inspiral, merger, and ringdown stage of merging black holes (a type of compact binary coalescence). Middle and bottom: a waveform simulation plotted using LALsim, with the middle one plotted in the time domain and the bottom one plotted in the frequency domain. The gravitational wave was idealized without any noise to show the shape of the wave. The waveform was plotted using the same parameters as GW190521 and IMRPhenomD waveform approximant.

still not enough for gravitational wave detection. LIGO uses more technology to further increase the sensitivity, which will be introduced later in this section. The laser used by LIGO is a 4W Laser light at 808nm [2, 3, 27, 29]. This near-infrared laser beam will then stimulate the emission of a 2W beam at a wavelength of 1064nm. The beam will later be amplified to 200W, and this beam will be sent into the detector. In order to reach the detection requirement of 750kW, power recycling mirrors were introduced. Inside each arm (between the power recycling mirror and the mirror), the laser beam is recycled about 300 times to pump up the effective power [28]. This recycling would also pump up the effective travelling length, which enlarged the distance travelled from 4km to 1200km. LIGO detectors also employ both active and passive vibration isolation systems [30] to try to reduce the noise to a minimal

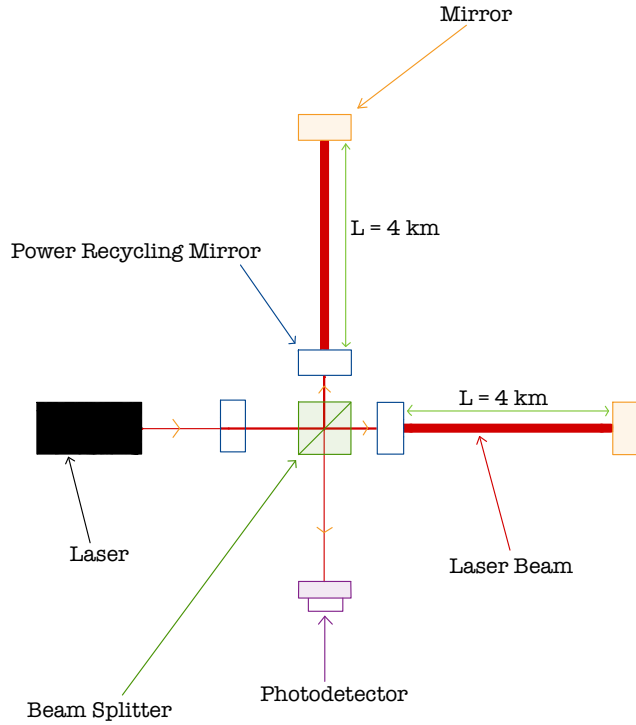


Figure 3. A schematic diagram of the LIGO detectors

amount, such as optics suspension and seismic isolation. All these factors contribute to the fact that current detectors could attain sensitivities of at least 10^{-19} m to detect incoming gravitational waves. The noise budgets and sensitivities of the advanced LIGO (aLIGO) detectors are presented in figure 4.

The beam splitter, mirrors, and power recycling mirror are all attached to test masses [32]. These test masses are free to swing in horizontal directions. When gravitational waves incident normally on the plane of the interferometer arms, one arm would be stretched while the other one would be contracted. Mathematically, if

$$\Delta L = L_x - L_y = n\lambda, \quad (8)$$

with L_x and L_y representing the arm length of the two arms, $n = 0, 1, 2, 3, \dots$ and λ is the wavelength of light passing into the detector, and then constructive interference would occur. On the other hand if

$$\Delta L = L_x - L_y = \left(n + \frac{1}{2}\right)\lambda, \quad (9)$$

destructive interference would occur. Any value of n between these 2 cases would lie between destructive and constructive

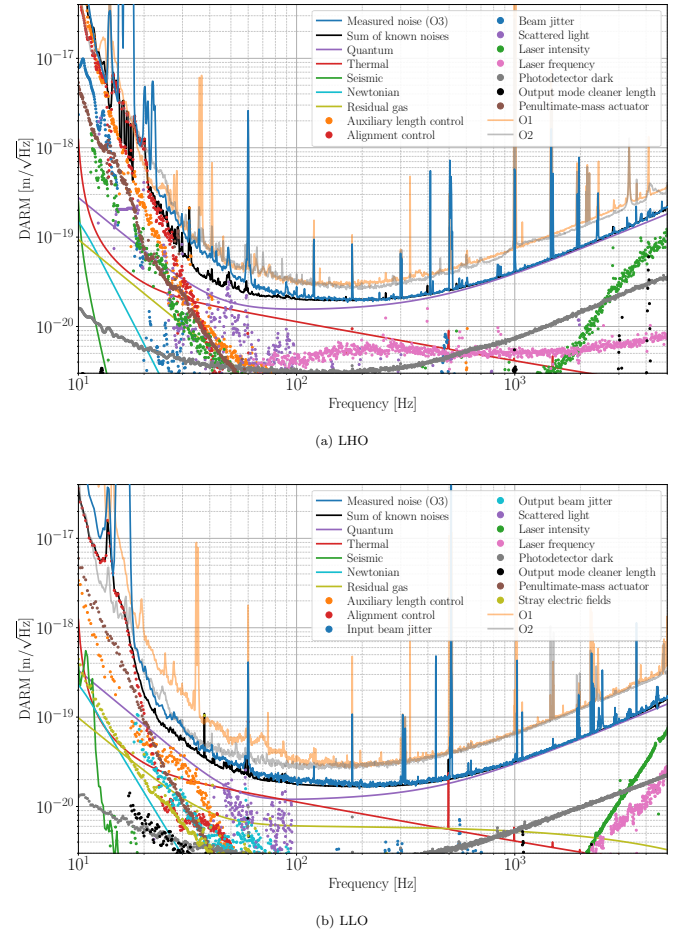


Figure 4. Total noise budget of (a) LIGO Handford Observatory (LHO) and (b) LIGO Livingston Observatory (LLO) [31]. The calculated noise terms are given in solid lines, while measured contributions are given as dots.

interference.

C. Searching and Data Analysis of Gravitational Waves

While many methods were employed to reduce noise in the detectors, the noise in the collected data is usually tremendous. A technique called matched filtering could be used to retrieve the real gravitational wave signal from all the noises. In a nutshell, matched filtering considers the correlation between the data and the template waveforms. Suppose a real gravitational wave is present in the data. In that case, the correlation between the two should be very high, given that the template matches the real gravitational wave and the amplitude should not be too small.

After the two hypotheses we need to consider [33]:

1. Null hypothesis \mathcal{H}_0 : There is only noise, so that $s(t) = n(t)$.

2. Signal hypothesis \mathcal{H}_1 : There are both noise and signal, so that $s(t) = n(t) + h(t)$

Where $s(t)$ is the signal recorded, $n(t)$ is the background noise and $h(t)$ is the gravitational wave signal.

Define inner product as

$$(a, b) = 4Re \int_0^\infty \frac{\tilde{a}(f)\tilde{b}^*(f)}{S(f)} df. \quad (10)$$

Then the signal-to-noise ratio (SNR) could be expressed as

$$\rho = \frac{(d, h)}{\sqrt{(d, h)}}, \quad (11)$$

with $d(t)$ representing the template waveform.

If it is assumed that the noise is Gaussian, it would be possible to compute the probability density. Under \mathcal{H}_0 , we have $n(t) = s(t)$, and so

$$p(s|\mathcal{H}_0) = p_n[s(t)] \propto e^{-\frac{(s,s)}{2}}. \quad (12)$$

Under \mathcal{H}_1 , we have $n(t) = s(t) - h(t)$, and so

$$p(s|\mathcal{H}_1) = p_n[s(t) - h(t)] \propto e^{-\frac{(s-h, s-h)}{2}}. \quad (13)$$

A new parameter called the likelihood ratio can be defined by the odd ratio for the alternative hypothesis given the observed data $s(t) = O(\mathcal{H}_1|s)$. Mathematically, it is written as:

$$\mathcal{L}(\mathcal{H}_1|s) = \frac{p(s|\mathcal{H}_1)}{p(s|\mathcal{H}_0)}, \quad (14)$$

where p is the probability density. Therefore we have,

$$\begin{aligned} \mathcal{L}(\mathcal{H}_1|s) &= \frac{e^{-\frac{(s-h, s-h)}{2}}}{e^{-\frac{(s,s)}{2}}} \\ &= e^{s,h} e^{-\frac{(h,h)}{2}} \end{aligned} \quad (15)$$

It could be observed that the likelihood ratio depends on $s(t)$ only through the inner product (s,h) . The inner product

$$(s, h) = 4Re \int_0^\infty \frac{\tilde{s}(f)\tilde{h}^*(f)}{S(f)} df \quad (16)$$

is called the matched filter, as it is a noise-weighted correlation of the anticipated signal with the data.

In reality, the likelihood ratio depends on many parameters [34] [20]. Therefore, it could be written explicitly as

$$\mathcal{L} = \frac{P(\vec{D}_H, \vec{O}, \vec{\rho}, \vec{\xi}^2, [\Delta\vec{t}, \Delta\vec{\phi}]|\vec{\theta}, \text{signal})}{P(\vec{D}_H, \vec{O}, \vec{\rho}, \vec{\xi}^2, [\Delta\vec{t}, \Delta\vec{\phi}]|\vec{\theta}, \text{noise})} \cdot \frac{P(\vec{\theta}|\text{signal})}{P(\vec{\theta}|\text{noise})}. \quad (17)$$

It can be observed that the likelihood ratio depends on the following:

1. Participating detectors \vec{O} .
2. Horizontal distances and hence the sensitivity of the detectors \vec{D}_H .
3. Matched filter Signal-to-Noise ratio (SNR) $\vec{\rho}$.
4. Signal consistency test value at each detector $\vec{\xi}^2$.
5. Time delay between detectors $\Delta\vec{t}$ (only for coincident events)
6. Phase difference between detectors $\Delta\vec{\phi}$ (only for coincident events)
7. The parameters of the templates $\vec{\theta}$

In practice, the value of \mathcal{L} could be very large or very small. Therefore, $\ln\mathcal{L}$ is usually used instead of \mathcal{L} alone. After the search, a list of candidates would be ranked according to the $\ln\mathcal{L}$ value.

False-alarm-probability (FAP) is the probability of pure noise to produce a trigger with a ranking statistic $\ln\mathcal{L}$ larger or equal to the ranking statistic of the trigger $\ln\mathcal{L}^*$. Mathematically, FAP could be written as

$$\text{FAP} = P(\ln\mathcal{L} \geq \ln\mathcal{L}^* | \text{noise}) = \int_{\ln\mathcal{L}^*}^{\infty} P(\ln\mathcal{L} | \text{noise}) d(\ln\mathcal{L}). \quad (18)$$

A low FAP means the probability of the signal being generated by pure noise is low, and vice versa. FAP is important to know as it is essential for calculating False-Alarm-Rate (FAR). FAR is another parameter used to compute the rate of how often would a pure noise produce a trigger with a ranking statistic $\ln\mathcal{L}$ larger or equal to the ranking statistic of the trigger $\ln\mathcal{L}^*$. Mathematically, FAR could be computed as

$$\text{FAR} = \frac{N \times \text{FAP}}{T}, \quad (19)$$

where N is the total number of observed candidates, and T is the duration of the data analyzed. In short, the higher the FAR, the lower the likeliness that the recorded event is a gravitational wave event, and vice versa.

After all these procedures, the final list of ranked candidates would be transferred to analysts for further analysis, such as using Bayesian methodology and posterior overlap analysis on the waveform [35]. If the event passed the analysis, it would be designated to be a new gravitational wave event.

Although, in theory, gravitational waves could be produced from other sources other than binary coalescence, the current sensitivity of our available detectors could only detect gravitational waves with relatively large amplitude (10^{-21}m) [26]. Therefore, contemporary detectors do not readily detect gravitational waves from other sources. As a result, this research would only focus on the lensing of gravitational

waves from compact binary coalescence.

Research focusing on searching gravitational waves signal has developed numerous search pipelines to search for possible candidates. It was already mentioned that numerous researchers are out there searching for gravitationally lensed counterparts of confirmed gravitational wave signals. However, it is confirmed that there are currently no gravitationally lensed pairs in the catalogue of detected gravitational waves [19]. To find other possible lensed pairs, lower signal-to-noise ratio signals that usually would not cause a trigger are required during the search as the first detected lensed image would most probably be a sub-threshold signal [19]. These possible gravitational wave signals are called sub-threshold gravitational waves, as their intensities are not high enough to reach the normal trigger threshold.

As mentioned before, this research employs GstLAL as our search pipeline. GstLAL is a pipeline built initially for gravitational wave detection but not lensed gravitational waves. However, it is possible for us to modify the pipeline to suit our requirement for sub-threshold gravitational lensing searching.

GstLAL is a gravitational wave signal-searching pipeline that utilises matched-filtering analysis technique. The matched-filtering technique is already mentioned in the previous section. The output of the matched-filter is the signal-to-noise ratio (SNR) [20], which is equivalent to the inner product of the whitened data with the whitened template. Whitening is required as several strong spectral lines always exist, which would severely affect the data analysis process. In the GstLAL pipeline, the calculations are performed in the time-domain. As a result, we have the following:

$$x_i(t) = \int_{-\infty}^{\infty} d\tau \hat{h}_i(\tau) \hat{d}(\tau + t), \quad (20)$$

where

$$\hat{d}(\tau) = \int_{-\infty}^{\infty} df \frac{\tilde{d}(f)}{\sqrt{S_n(|f|)/2}} e^{2\pi i f \tau} \quad (21)$$

is the whitened data, and the whitened template $\hat{h}_i(\tau)$ is defined similarly. Here the accent \tilde{x} represents the corresponding Fourier-transformed frequency of function x , and \hat{y} represents the whitened data of the series y . The subscript i represents the process running over each template parameter set in the template bank. $S_n(f)$ is the single-sided noise power spectral density (PSD).

Gravitational waves generally consist of two polarisations. Therefore, there would be two real waveforms for each set of parameters in the template bank. One waveform corresponds to the + polarization, and the other corresponds to a "quadrature phase-shifted +" waveform, which is equal to the \times polarization barring an overall amplitude factor. Now a complex SNR time series $z(t)$ would be able to be constructed with the real part being the + polarized template($x_i(t)$) and

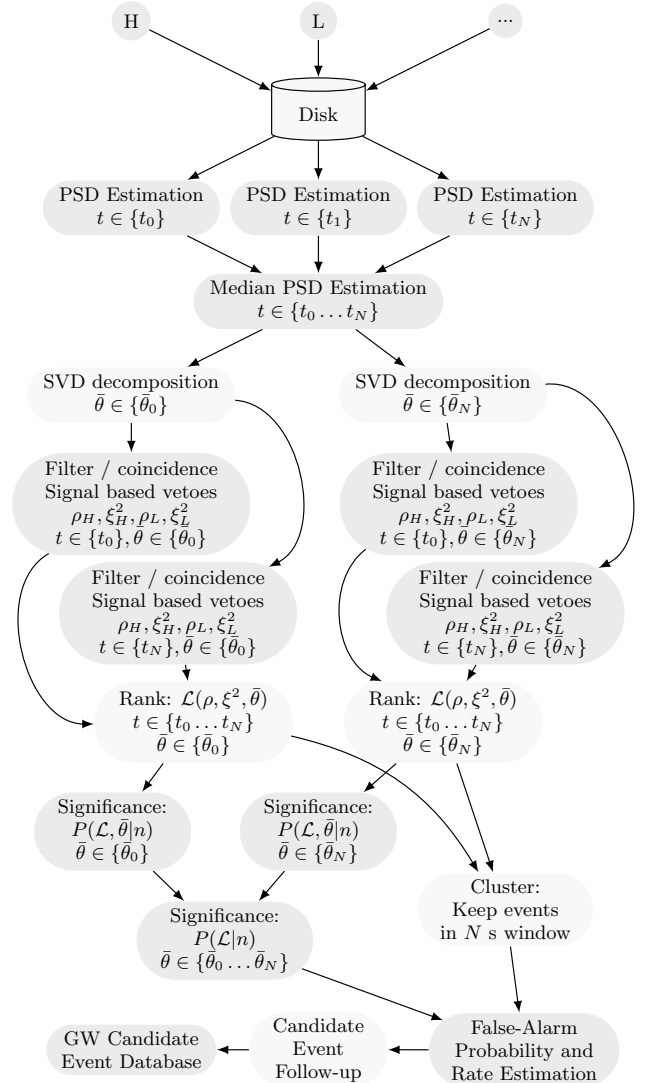


Figure 5. A flowchart of GstLAL pipeline [36]

the complex part being the "quadrature phase-shifted +" template($y_i(t)$). So that we have

$$z(t) = x_i(t) + iy_i(t). \quad (22)$$

Real-world data collected from the detected often contain glitches from various sources. These glitches would produce high peaks in the SNR time series as the peaks are similar to the waveform at the merger phase. SNR alone is inadequate to distinguish noise from transient signals in the presence of non-Gaussian data. To tackle the issue, GstLAL performs a signal consistency test whenever it records an SNR above a certain threshold. ξ^2 is the signal consistency test value. It

could be calculated by

$$\xi^2 = \frac{\int_{-\delta t}^{\delta t} dt |z(t) - z(0)R(t)|^2}{\int_{-\delta t}^{\delta t} dt |2 - 2R(t)|^2}, \quad (23)$$

where $z(t)$ is the SNR time series, $z(0)$ is the peak, $R(t)$ is the auto-correlation series and δt is the time window around the peak. The auto-correlation series is calculated by the auto-correlation between the complex template waveform and itself, then scaling it by the peak of the peak complex SNR.

When the GstLAL pipeline records a peak in the SNR time series greater than a preset threshold, it will record the SNR, ξ^2 , the masses, and the spins of the templates, which the above values would be returned upon matched filtering, the phase and finally the time of the coalescence. Altogether, these recorded parameters form a trigger. These triggers would then be assigned a log likelihood ratio and the FAP (see the previous section for a more detailed description).

On-going research on searching these sub-threshold lensed counterparts usually focuses on the similarity between the waveform of the possible signals and the confirmed gravitational waves, as the morphology of different lensed images would be the same except for differences in magnifications, arrival time, and phase shifts [34]. The sky locations of the incoming waves are not restricted in the search pipeline. This research aims to modify the terms relating to the sky location restrictions of the signals in the searching pipeline to increase the accuracy further and narrow down the possible candidates to facilitate further analysis of possible gravitationally lensed pairs.

D. Gravitational Lensing

From Einstein's field equation expressed in equation 1, we can see that space-time is curved around massive objects such as black holes or galaxy clusters. As light travels at the speed of light, it travels in null geodesic such that proper time cannot be defined. In this case, a new parameter called affine parameter λ could be used. As a result, we can define a velocity like vector

$$\vec{v}_\lambda = \frac{dx}{d\lambda} \quad (24)$$

such that the geodesic equation

$$\frac{dv^\alpha}{d\tau} = -\Gamma_{\mu\nu}^\alpha v^\mu v^\nu \quad (25)$$

is still valid. By putting equation 24 into equation 25, we can obtain

$$\frac{dv_\lambda^\alpha}{d\tau} = -\Gamma_{\mu\nu}^\alpha v_\lambda^\mu v_\lambda^\nu. \quad (26)$$

By applying equation 26, the paths of light in curved space-time could be found.

As a toy example, we consider space-time around spherical celestial bodies using the Schwarzschild metric, as the majority of the celestial bodies are nearly spherical due to gravity. The Schwarzschild metric is a metric to describe a spherically symmetric curved space-time. Therefore, by substituting the Schwarzschild metric in spherical coordinate

$$g_{\mu\nu} = \begin{bmatrix} -(1 - \frac{2M}{r}) & 0 & 0 & 0 \\ 0 & (1 - \frac{2M}{r})^{-1} & 0 & 0 \\ 0 & 0 & r^2 & 0 \\ 0 & 0 & 0 & r^2 \sin^2(\theta) \end{bmatrix} \quad (27)$$

as metric tensor, we can find the Christoffel symbols by using the relation

$$\Gamma_{\beta\gamma}^\delta = \frac{1}{2g_{\alpha\delta}} \left(\frac{dg_{\alpha\beta}}{dx^\gamma} + \frac{dg_{\alpha\gamma}}{dx^\beta} - \frac{dg_{\beta\gamma}}{dx^\alpha} \right). \quad (28)$$

Putting equation 28 back to equation 26 would allow us to obtain

$$\frac{dv_\lambda^r}{d\lambda} = (r - 3M)(v_\lambda\phi)^2 \quad (29)$$

and

$$v_\lambda\phi \propto \frac{1}{r^2}. \quad (30)$$

Therefore, the path of light around a massive object is bent. In other words, massive objects at or near the path of propagation act as a "gravitational lens" to bend the propagation direction of light.

The effect of gravitational lensing predicted by general relativity is illustrated visually in figure 6. As the lights from the source travel through several different paths to reach the observer on Earth, multiple images with different arrival time could be observed.

It is possible to derive the image positions and image brightness using thin lens approximations. The deflection angle α for a light ray passing by a mass M at an impact parameter $b \gg M$ is given by

$$\alpha = \frac{4M}{b} \equiv \frac{2R_S}{b}, \quad (31)$$

where α is the deflection angle, R_S is the Schwarzschild radius, which is equal to

$$R_S = \frac{2M}{c^2}. \quad (32)$$

Besides, all deflection is assumed to be on the normal plane of the line of sight of the gravitational lens. Thin lens approximations could be used with great accuracy as light travels in a straight line in most of the journey except when passing around the gravitational lens. Therefore, we can treat the lens as a point in space, which is the thin lens approximation.

lens

By the equivalence principle, since gravitational waves and electromagnetic waves are both waves propagating at the speed of light, the lensing of gravitational waves should have the same effect as electromagnetic waves.

This research would focus on images produced by strong lensing only. The properties of strong lensing include the following [34]

1. Relatively large arrival time difference Δt between images.
2. No overlapping of images due to large Δt and short signal duration of gravitational waves for binary blackhole mergers. Overlapping might occur for binary neutron star mergers as the signal may last for 30 seconds or more [7].
3. Intensity of different images would be different.
4. The amplification factor is frequency-independent (i.e. achromatic), which means all images retain the same waveform although they have different amplitudes.
5. Additional Morse phase factor.

III. METHOD

The plan to modify the TESLA pipeline [34] for lensing searches includes modifying the terms included in calculating the likelihood ratio in equation 17. The 2 terms being modified in the calculation are $\Delta\vec{t}$ and $\Delta\vec{\phi}$. These terms serve the purpose of restricting the sky location of the lensing images. The current sky location uncertainty of the source of the detected gravitational waves is in order of degree [7]. However, the difference in the sky locations of different lensed images is in the order of arc-second [15] which is much smaller than the uncertainty. Therefore, we can assume that different lensed images should come from similar sky locations. By adding the parameters corresponding to the sky locations of the gravitational images, the likelihood ratio would now also consider how likely the 2 gravitational waves came from the same sky location, hence ranking down the candidates that could not be possible to be the lensed counterpart of the detected signal.

Δt is the difference in arrival time of coincident triggers at different detectors [20]. Δt for a signal depends only on the position of the source and the location of the observatories. $\Delta\phi$ is the difference in the coalescence phase between H1 and L1 triggers, with $\Delta\phi \in [-\pi, \pi]$. Therefore, it is obvious that these terms could serve the purpose of restricting sky location. The relationship between Δt , $\Delta\phi$ and the source's sky location is illustrated in figure 9

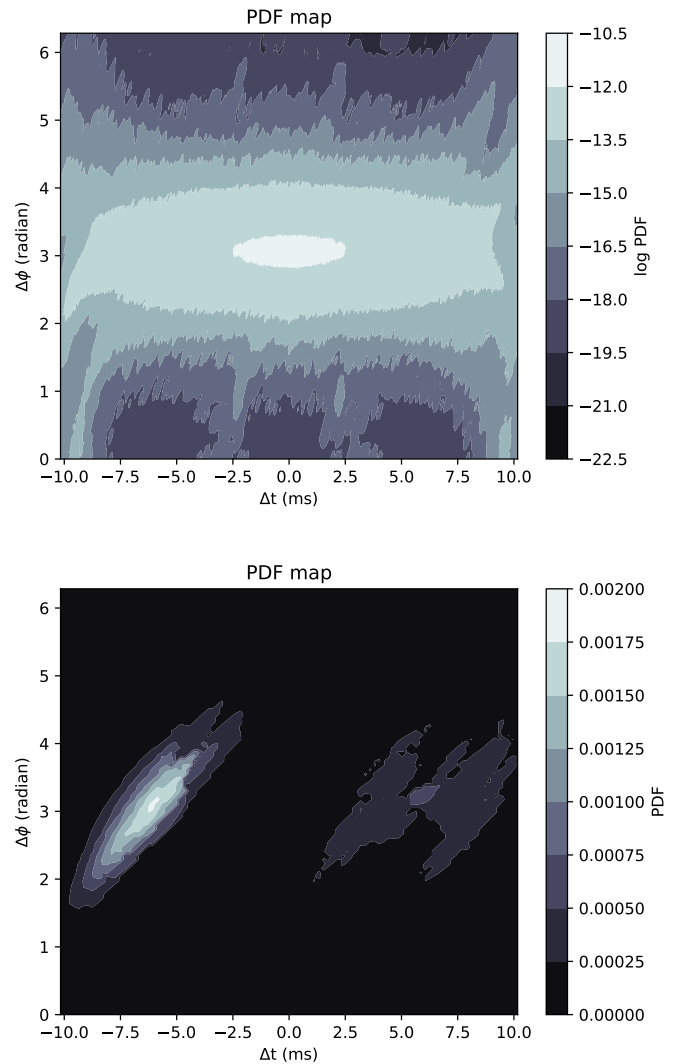


Figure 8. Top: Distribution of $P(\Delta\phi|\Delta t, \rho_{\text{network}})$ modified from [20]. Bottom: Distribution of $P(\Delta\phi|\Delta t, \rho_{\text{network}})$ after adding sky localisation constraints. The event used in this plot is GW190519.

We could model the Δt distributions as a function of a ratio of SNRs normalized by horizon distances, to factor out the inherent sensitivities of the detectors, so this term only depends on the position of the source concerning the detectors. Furthermore, we would define it such that it is always smaller than 1,

$$\rho_{\text{ratio}} = \min\left(\frac{\rho_{H1}/D_{H1}}{\rho_{L1}/D_{L1}}, \frac{\rho_{L1}/D_{L1}}{\rho_{H1}/D_{H1}}\right). \quad (37)$$

On the other hand, we do not need to consider the dependence on the detector sensitivities when modeling the $\Delta\phi$ distribution. We only need to consider the dependence of $\Delta\phi$ on Δt and network SNR, which is defined as

$$\rho_{\text{network}} = \sqrt{\rho_1^2 + \rho_2^2}. \quad (38)$$

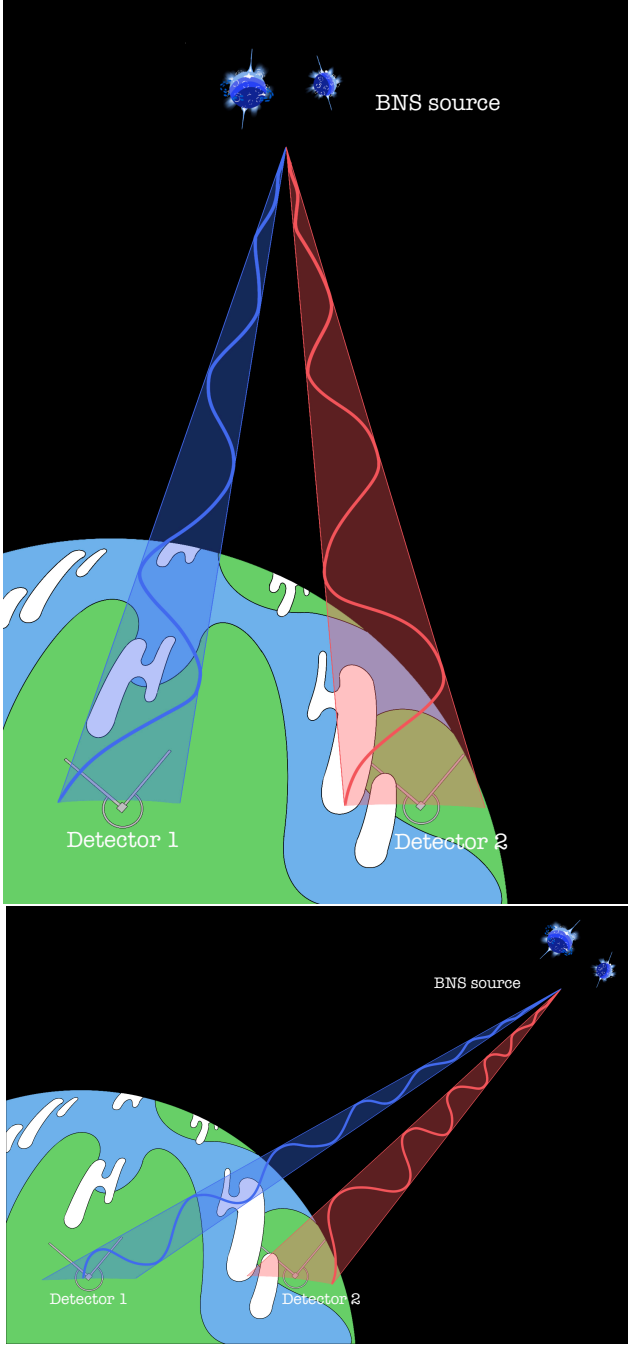


Figure 9. Top: The source is nearly perpendicular to the axis of the 2 detectors. Their arrival times and phases observed by the 2 detectors are nearly identical. Bottom: the source is at an angle to the axis of the detectors. Their arrival time and phases observed by the 2 detectors are different.

In figure 8, it shows the logarithm of the probability density function for $P(\Delta\phi|\Delta t, \rho_{\text{network}}, \text{signal})$. The top diagram is the original distribution while the bottom diagram is what the distribution would look like after the modification. As the sky location would be restricted for lensing searches, the contour lines representing $\ln P(\Delta\phi|\Delta t, \rho_{\text{network}})$ would be packed significantly closer together. As a result, it would affect the

likelihood ratios of the candidates so that we could rank the candidates according to their new likelihood ratios.

To perform the calculation quickly and efficiently, GstLAL employs certain mathematical methods to reduce the computational costs [37]. Firstly, the calculation of the likelihood ratio can be written as

$$\mathcal{L} = \frac{P(\vec{D}_H, \vec{O}, \vec{\rho}, \vec{\xi}^2, \vec{t}, \vec{\phi} | \text{signal})}{P(\vec{D}_H, \vec{O}, \vec{\rho}, \vec{\xi}^2, \vec{t}, \vec{\phi} | \text{noise})}. \quad (39)$$

The numerator can be factorized as with "s" representing "signal"

$$\begin{aligned} P(\vec{D}_H, \vec{O}, \vec{\rho}, \vec{\xi}^2, \Delta\vec{t}, \Delta\vec{\phi} | s) &= P(\vec{D}_H | s) \times P(\vec{O} | \vec{D}_H, s) \\ &\quad \times P(\vec{\xi}^2 | \vec{\rho}, s) \\ &\quad \times P(\vec{\rho}, \vec{\phi}, \vec{t} | \vec{O}, \vec{D}_H, s). \end{aligned} \quad (40)$$

By replacing ρ with effective distances $\vec{D}_{eff} =$, we have

$$P(\vec{\rho}, \vec{\phi}, \vec{t} | \vec{O}, \vec{D}_H, s) \propto P(\ln \Delta \vec{D}_{eff}, \Delta \vec{\phi}, \Delta \vec{t} | \vec{O}, s) \times |\rho|^{-4}. \quad (41)$$

To simplify the situation, we can define a vector $\vec{\lambda}$ such that

$$\vec{\lambda} \equiv [\Delta \ln \vec{D}_{eff}, \Delta \vec{\phi}, \Delta \vec{t}]. \quad (42)$$

In order to construct the distribution of these parameters for a signal, a uniform distribution of gravitational waves in Earth-based coordinates was asserted. They are, namely: right ascension α , declination $\cos(\delta)$, inclination angle $\cos(\iota)$, and polarization angle Φ . A uniform, densely sampled grid in $[\alpha, \cos(\delta), \cos(\iota), \cos(\delta)]$ could be formed and further assert that any signal should "exactly" land on one of the grid points. The grid is then transformed to a grid of irregularly spaced points in $\vec{\lambda}$, which is denoted as $\vec{\lambda}_{mi}$ for the i^{th} model vector.

After using covariance matrix, Fisher information matrix, and Cholesky decomposition for simplifications, the probability distribution now becomes

$$P(\lambda | \vec{O}, s) \approx \exp\left[-\frac{1}{2} \Delta \vec{x}_0^2\right] \times \sum_i \exp\left[-\frac{1}{2} g_{0i}^2\right], \quad (43)$$

where $\Delta \vec{x}_0$ refers to the distance between the candidate parameter and the nearest-neighbour grid point, and g_{0i} is the distance between the i^{th} grid point to the nearest grid point. Since the entire sum over i term can be precomputed and stored, it would allow a fast and efficient evaluation during the observing runs.

IV. PROCEDURES

A. Skymap Plotting

The sky location of the target used in targeted lensing search would be used for calculating the $P(\Delta t, \Delta\phi)$. Therefore, it is necessary to extract the data from the skymaps of

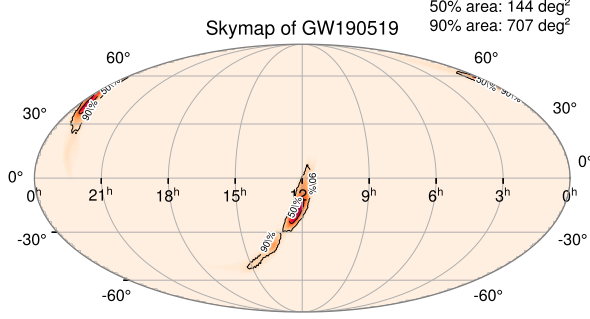


Figure 10. Sky location of GW190519 using IMRPhenomD waveform approximant.

gravitational events, particularly the 90% credible region of the target gravitational wave. This could be achieved by using `ligo.skymap`, and `healpy` to read and plot the skymap data as a new skymap. One of the skymaps plotted is shown below in fig 10.

B. inspiral_dtdphi.h5 file generation

In order to calculate the $P(\Delta t, \Delta \phi)$ PDF map for a targeted search, an `inspiral_dtdphi.h5` file containing the sky location of the target, SNR, and PSD (noise budgets) of the detectors is required.

The characteristic SNRs of the detectors could be found in Hanna’s paper [37]. The noise budgets of detectors could be found on LIGO GitLab written in `xml.gz` format. In order to supply only one `xml.gz` file to the pipeline, a new programme was written to combine all the `xml.gz` files from each of the detectors. The final product was plotted out and is shown in fig 11.

C. Calculate the probability density

After generating the `.h5` file, The probability density of each possible combination of Δt and $\Delta \phi$ can be calculated using `gstlal.inspiral.extrinsic.TimePhaseSNR`. There are no dedicated plotting script for $P(\Delta t, \Delta \phi)$, so a new python script was written to plot out the desired graph.

The code was written in a way that it can accept several parser arguments such as the `.xml` document, `.h5` file, choices for detectors (choosing 2 detectors each time), the pixel density of the PDF map, and the SNR of the detectors. One

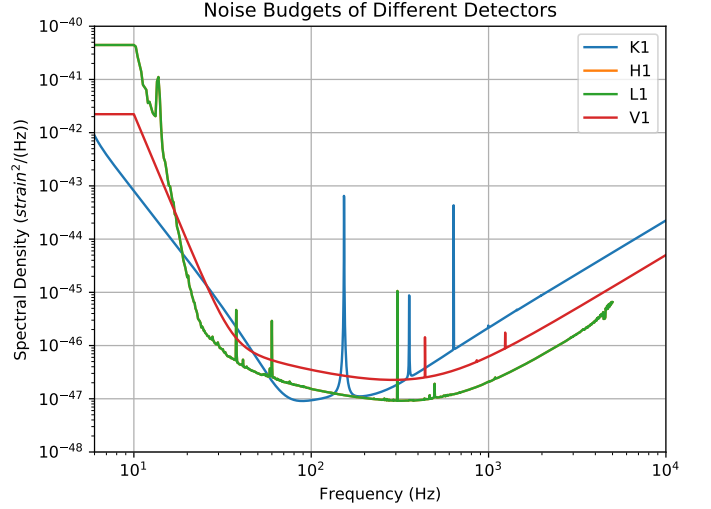


Figure 11. The noise budgets of the detectors plotted using my own written code.

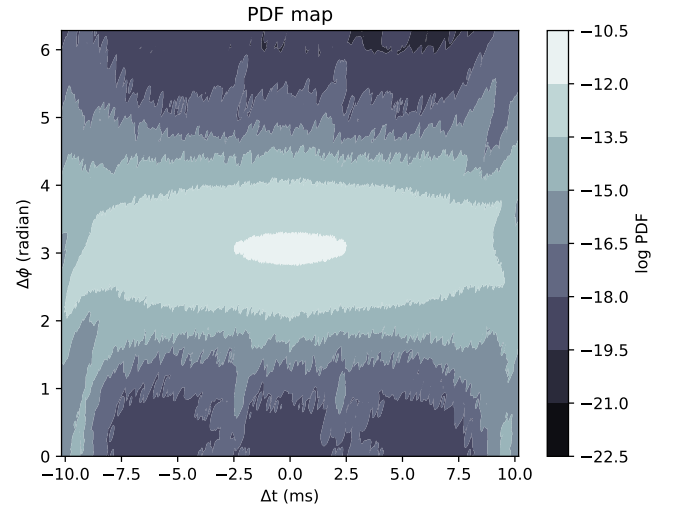


Figure 12. A PDF graph plotted using my own code. The parameters are as follow: Detectors used = H1 and L1, Horizon distance = 100Mpc, SNR of both detectors = 10.

of the plotted PDF graph is shown below in fig 12.

D. Tiling the Sky

The new pipeline is required to load in a skymap and calculate the PDF using the given sky location when performing targeted searches, but the vanilla `GstLAL` function does not include the argument of inputting a skymap. Therefore, in order for making the software to allow the input

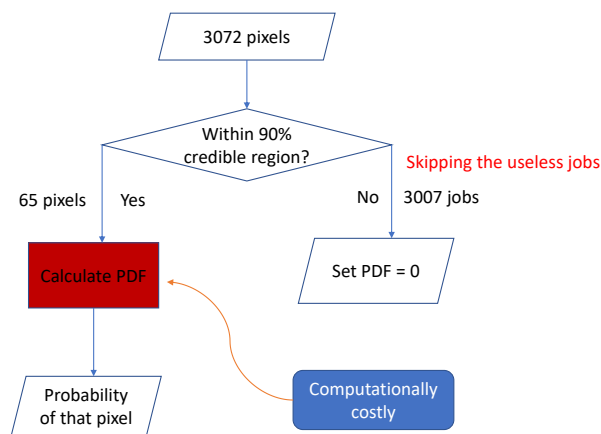


Figure 13. A float chart showing the program flow of the new pipeline when targeted search function is enabled.

of a skymap argument, some of the files including both executables and python scripts have to be modified. The files changed include: `gstlal_inspiral_compute_covmat`, `gstlal_inspiral_create_dt_dphi_snr_ratio`, `gstlal_inspiral_create_dt_dphi_snr_ratio_dag`, and `gstlal_inspiral_extrinsics.py`.

The code was modified such that it can now select the 90% credible of the target event. The probability density would be re-distributed if targeted search was enabled. The new probability density would be uniformly distributed among the 90% credible region and 0 anywhere else. The issue of extreme inefficiency was solved by only calculating the relevant pixels within the 90% credible region. The end result is the reduction of jobs from 3072 jobs to 67 jobs for the event GW190519, which allows the calculation to be finished within 2 hours. The float chart of the modified pipeline is shown in 13.

I have successfully generated the PDF map of GW190519, and it is shown in 14.

E. Rotation of the Earth

The Earth is constantly rotating. As lensing might cause a delay in time between images in the order of months, we have to account for the change in orientations of ground-based detectors when the lensed images arrive. Since each targeted search can produce more than 10000 triggers, it would be inefficient to generate each rotated-PDF map for each trigger. The solution would be to generate several hundreds of PDF maps for each targeted search, each with a slight difference in rotation angles representing a difference in arrival time. During the actual search, the trigger would be paired with a PDF map which has the most similar arrival time as the trigger and does the calculation.

In order to achieve this, several skymaps rotated with different angles using `healpy.rotator.Rotator` were prepared, and

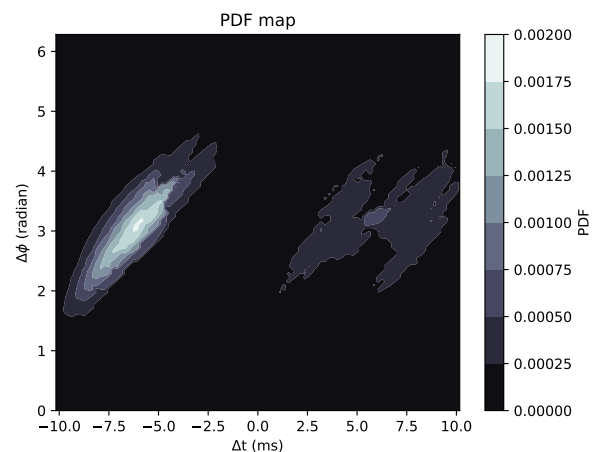


Figure 14. A PDF graph of GW190519 event plotted using my own code. The parameters are as follow: Detectors used = H1 and L1, SNR of both detectors = 10.

were plotted out using the PDF plotting script. The result is shown in 15.

F. Determine the number of required skymaps

In theory, a new PDF map could be generated specifically for a trigger that could exactly match the trigger time. However, for 1 targeted search, the number of triggers generated would be in the order of 10000, which makes generating new PDF maps on the run extremely inefficient. The solution would be to generate a finite number of PDF maps for rotating through a sidereal day, and then assign suitable PDF maps for the analysis according to the trigger time.

The requirement for the determination of the number of PDF maps needed is that the minimum overlapping percentage of the 90% credible region of adjacent PDF maps is larger than 80%. It was found that by rotating 720 steps per sidereal day, the minimum overlapping area was 82.2% (for event GW190519), the variation of the overlapping percentage over 1 sidereal day rotation was shown in 16. As a result, for every targeted search, 720 was chosen to be the number of PDF maps required for the pipeline.

G. Implementation into GstLAL

It is true that the area of the 90% credible region would be dependent on how localised the event is. Therefore, it is highly likely that different events would have slightly different minimum overlapping area even if the number of steps per rotation is the same. A pessimistic approach was chosen in order to tackle this issue.

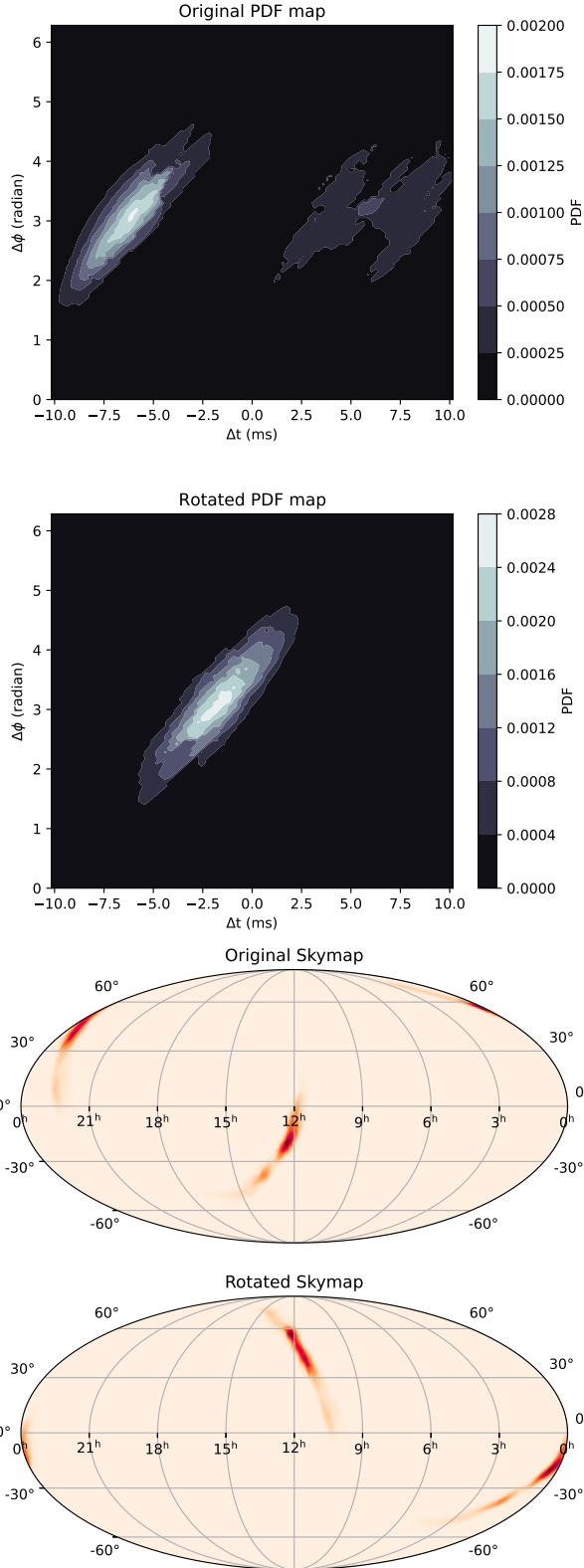


Figure 15. Top 1: The original PDF map of GW190519. Top 2: PDF map of GW190519 after a 180 degrees rotation of the skymap. Bottom 1: The original skymap of GW190519. Bottom 2: The skymap of GW190519 after a 180 degrees rotation from the original skymap

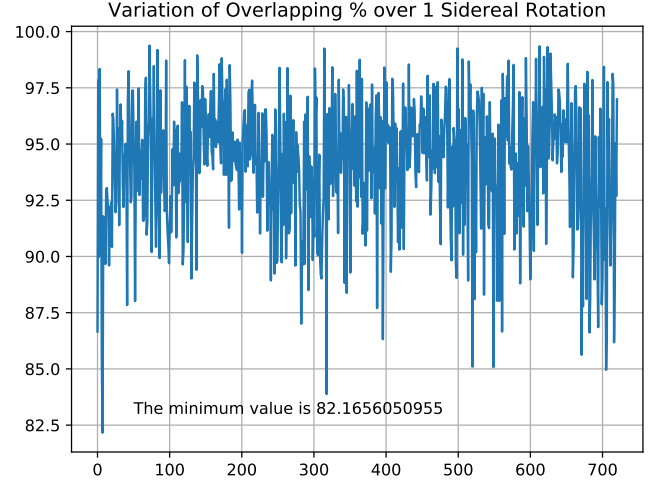


Figure 16. A graph showing the variation of the overlapping percentage of the PDF maps by rotating the map 720 times per cycle of GW190519 event over 1 sidereal day rotation.

For every trigger, we would assign the 2 closest PDF map in time for the analysis. 2 likelihood ratios would be calculated at the end, and the pipeline would assign the one with a more significant value as the likelihood of the trigger. It was chosen this was because it would be undesirable if we down rank an actual trigger, we would like to retrieve as much real triggers as possible.

The float chart of how this modified method is incorporated into GstLAL is shown in 17.

V. FUTURE PLANS

A. Completing the test

Currently, I am using both the vanilla GstLAL and my modified GstLAL to search through data from GW190512 to GW190519 while using GW190519 event as the target. Since doing a complete search would take a lot of time, it is probably not going to be completed before the submission deadline. After getting the result, I would compare how the likelihood ratios of several real events would be changed if I used the targeted search function. Real events having very different sky locations as GW190519 should be down ranked significantly.

C. Further Applications

Implementation

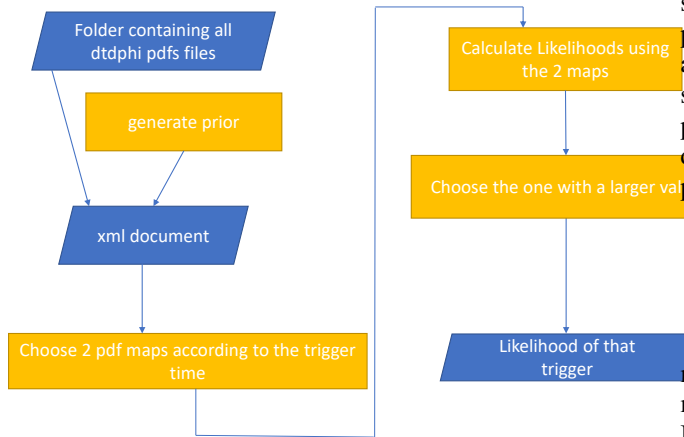


Figure 17. Firstly, all 720 PDF maps would be stored in a folder. The file path would be stored into an xml document together with the priors. Then it would be passed into another script to calculate the likelihood ratio. 2 PDF maps would be used and the one with a higher likelihood would be assigned as the likelihood of the trigger.

B. Mock Data Challenge

If the aforementioned testing goes successfully, with events having different sky locations down ranked significantly, it would be possible to proceed to perform a mock data challenge.

For a mock data challenge it can either be performed using a real event or a simulated event (with a simulated sky location) as the target. Copies of these target signals with a reduction in amplitude to simulate sub-threshold counterparts would be injected into the data. Lastly, the prepared data stream would be searched by both vanilla GstLAL and my modified GstLAL pipeline.

The aim of a mock data challenge would be to firstly test for how many injections we could retrieve using the 2 pipelines, and secondly, to test for the efficiency of both pipelines. We can look for parameters such as the number of real injections retrieved compared to the number of noise triggers with the same ranking statistic threshold and False Alarm Rates of the real injections before and after the implementation of the sky location-constrain method.

If the modified pipeline works efficiently and could successfully rank up real sub-threshold triggers, then it could be incorporated into the official GstLAL.

There are other astrophysical phenomena that this targeted search method would be applicable to be applied. For example, if we detected a Gamma Ray Burst that might come from a binary neutron star merger, we might use a similar targeted search technique to search for the gravitational wave counterpart. The same goes for supernovae if the sensitivity of the detectors allows the detection of gravitational waves from supernovae.

VI. ACKNOWLEDGEMENT

The author would like to use this opportunity to thank all my mentors for their guidance and help throughout the summer. This project would not be possible without them. Lastly, I would like to thank National Science Foundation, LIGO Scientific Collaboration, Caltech SFP and CUHK Physics Department for granting me such an exceptional and invaluable research opportunity.

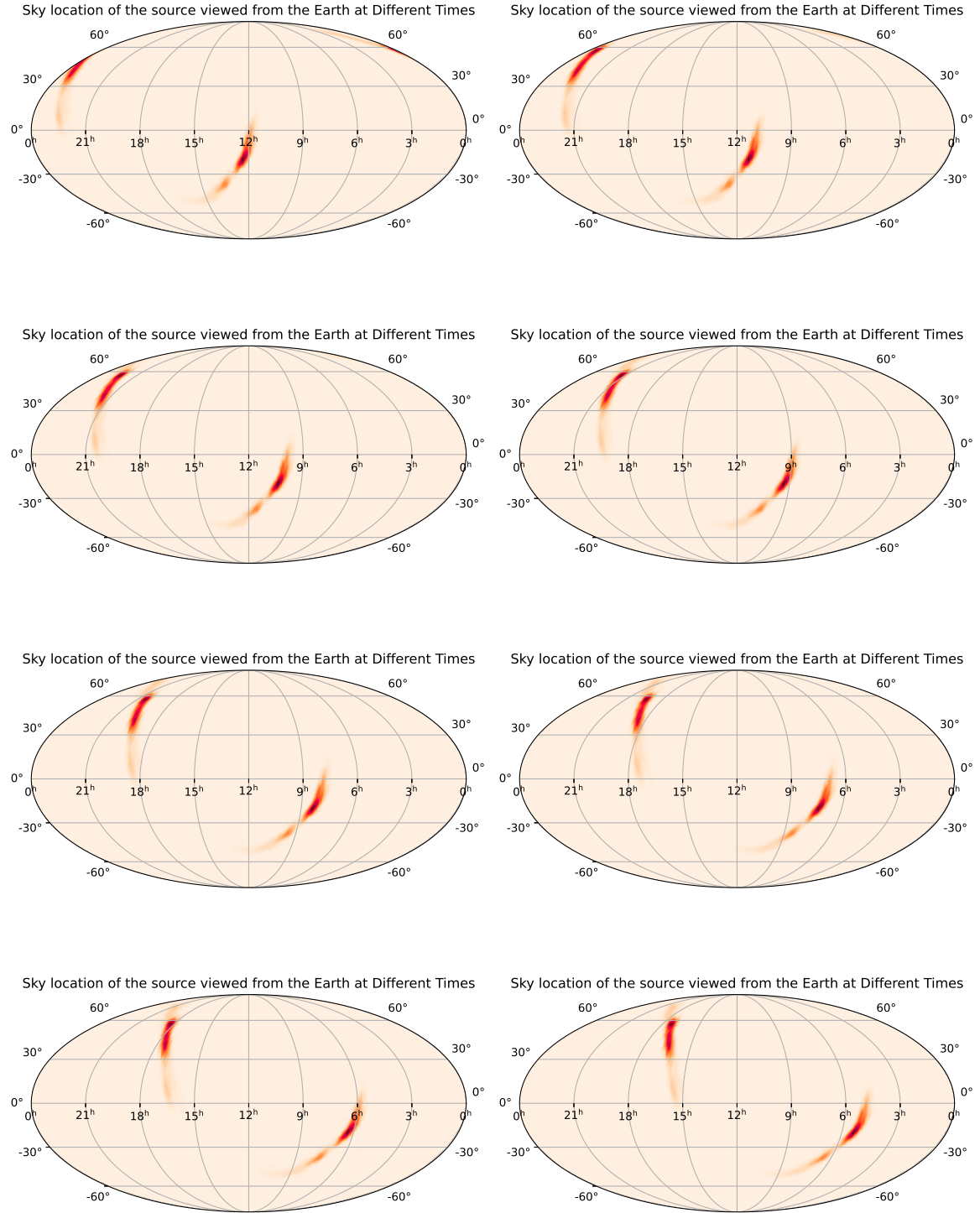
VII. REFERENCES

[t]

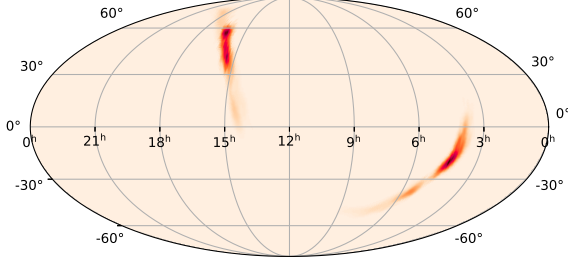
-
- [1] A. Einstein, Sitzungsber. Preuss. Akad. Wiss. Berlin (Math. Phys.) **1915**, 778 (1915), [Addendum: Sitzungsber.Preuss.Akad.Wiss.Berlin (Math.Phys.) 1915, 799–801 (1915)].
- [2] B. P. Abbott *et al.* (LIGO Scientific, Virgo), Phys. Rev. Lett. **116**, 061102 (2016), arXiv:1602.03837 [gr-qc].
- [3] R. Abbott *et al.* (LIGO Scientific, VIRGO, KAGRA), (2021), arXiv:2111.03634 [astro-ph.HE].
- [4] B. P. Abbott *et al.* (LIGO Scientific, Virgo), Phys. Rev. X **9**, 031040 (2019), arXiv:1811.12907 [astro-ph.HE].
- [5] R. Abbott *et al.* (LIGO Scientific, Virgo), Phys. Rev. X **11**, 021053 (2021), arXiv:2010.14527 [gr-qc].
- [6] R. Abbott *et al.* (LIGO Scientific, VIRGO, KAGRA), (2021), arXiv:2111.03606 [gr-qc].
- [7] B. P. Abbott *et al.* (LIGO Scientific, Virgo), Phys. Rev. Lett. **119**, 161101 (2017), arXiv:1710.05832 [gr-qc].
- [8] B. T. Reed, A. Deibel, and C. J. Horowitz, Astrophys. J. **921**, 89 (2021), arXiv:2104.00771 [astro-ph.HE].
- [9] N. Andersson, Universe **7**, 97 (2021), arXiv:2103.10223 [gr-qc].
- [10] F. Pretorius and W. E. East, Phys. Rev. D **98**, 084053 (2018), arXiv:1807.11562 [gr-qc].
- [11] T. Nakama, J. Silk, and M. Kamionkowski, Phys. Rev. D **95**, 043511 (2017), arXiv:1612.06264 [astro-ph.CO].
- [12] A. I. Renzini, B. Goncharov, A. C. Jenkins, and P. M. Meyers, Galaxies **10**, 34 (2022), arXiv:2202.00178 [gr-qc].
- [13] B. P. Abbott *et al.* (LIGO Scientific, Virgo, VIRGO), Astrophys. J. **909**, 218 (2021), [Erratum: Astrophys.J. 923, 279 (2021)], arXiv:1908.06060 [astro-ph.CO].
- [14] B. P. Abbott *et al.* (LIGO Scientific, Virgo, 1M2H, Dark Energy Camera GW-E, DES, DLT40, Las Cumbres Observatory, VINROUGE, MASTER), Nature **551**, 85 (2017), arXiv:1710.05835 [astro-ph.CO].
- [15] J. B. Hartle, *Gravity* (Cambridge University Press, 2021).
- [16] T. Broadhurst, J. M. Diego, and G. F. Smoot, (2019), arXiv:1901.03190 [astro-ph.CO].
- [17] L. Dai, B. Zackay, T. Venumadhav, J. Roulet, and M. Zaldarriaga, (2020), arXiv:2007.12709 [astro-ph.HE].
- [18] L. P. Singer, D. A. Goldstein, and J. S. Bloom, (2019), arXiv:1910.03601 [astro-ph.CO].
- [19] R. Abbott *et al.* (LIGO Scientific, VIRGO), Astrophys. J. **923**, 14 (2021), arXiv:2105.06384 [gr-qc].
- [20] S. Sachdev *et al.*, (2019), arXiv:1901.08580 [gr-qc].
- [21] F. Aubin *et al.*, Class. Quant. Grav. **38**, 095004 (2021), arXiv:2012.11512 [gr-qc].
- [22] Q. Chu *et al.*, Phys. Rev. D **105**, 024023 (2022), arXiv:2011.06787 [gr-qc].
- [23] S. A. Usman *et al.*, Class. Quant. Grav. **33**, 215004 (2016), arXiv:1508.02357 [gr-qc].
- [24] A. Einstein, Annalen Phys. **17**, 891 (1905).
- [25] B. P. Abbott *et al.* (LIGO Scientific, Virgo, Fermi-GBM, INTEGRAL), Astrophys. J. Lett. **848**, L13 (2017), arXiv:1710.05834 [astro-ph.HE].
- [26] “What is an interferometer?” .
- [27] “Ligo technology,” ().
- [28] “Ligo’s interferometer,” ().
- [29] “Ligo’s laser,” ().
- [30] “Vibration isolation,” ().
- [31] A. Buikema *et al.* (aLIGO), Phys. Rev. D **102**, 062003 (2020), arXiv:2008.01301 [astro-ph.IM].
- [32] “Ligo optics,” ().
- [33] J. D. E. Creighton and W. G. Anderson, *Gravitational-wave physics and astronomy: An introduction to theory, experiment and data analysis* (2011).
- [34] A. K. Y. Li, R. K. L. Lo, S. Sachdev, C. L. Chan, E. T. Lin, T. G. F. Li, and A. J. Weinstein, (2019), arXiv:1904.06020 [gr-qc].
- [35] J. Janquart, O. A. Hannuksela, H. K., and C. Van Den Broeck, Mon. Not. Roy. Astron. Soc. **506**, 5430 (2021), arXiv:2105.04536 [gr-qc].
- [36] C. Messick *et al.*, Phys. Rev. D **95**, 042001 (2017), arXiv:1604.04324 [astro-ph.IM].
- [37] C. Hanna *et al.*, Phys. Rev. D **101**, 022003 (2020), arXiv:1901.02227 [gr-qc].

VIII. APPENDIX

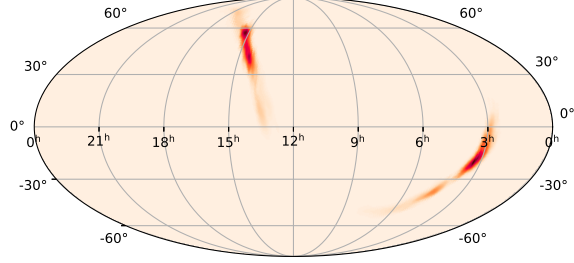
A. Rotation of GW190519 skymap in 24 hours (one map for each hour)



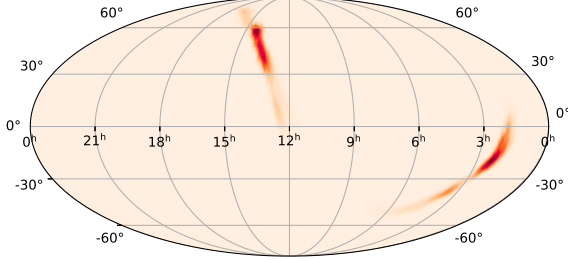
Sky location of the source viewed from the Earth at Different Times



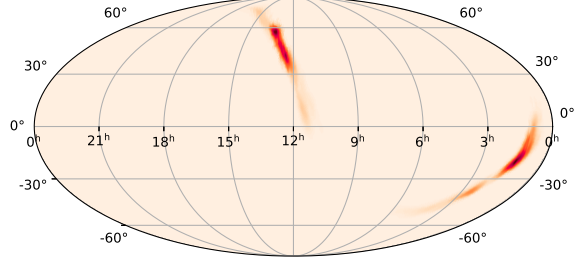
Sky location of the source viewed from the Earth at Different Times



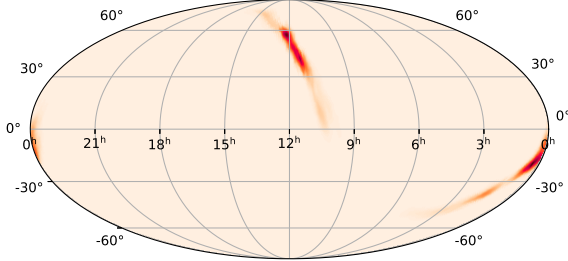
Sky location of the source viewed from the Earth at Different Times



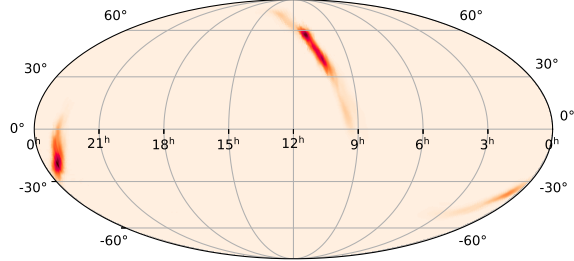
Sky location of the source viewed from the Earth at Different Times



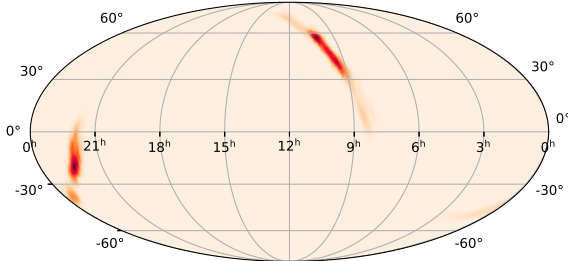
Sky location of the source viewed from the Earth at Different Times



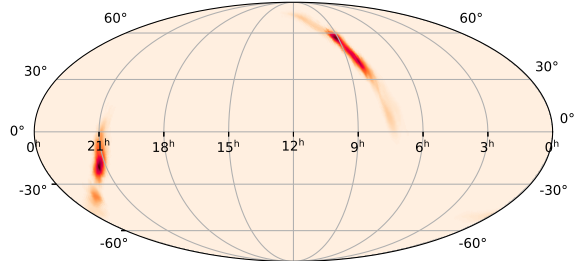
Sky location of the source viewed from the Earth at Different Times



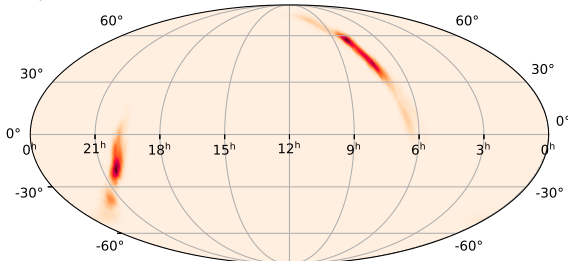
Sky location of the source viewed from the Earth at Different Times



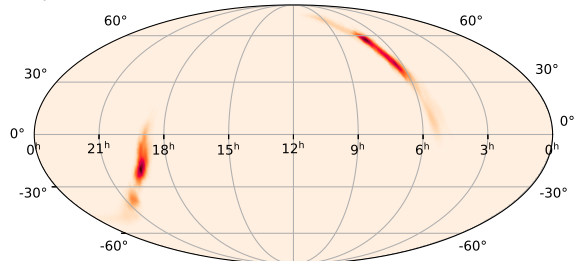
Sky location of the source viewed from the Earth at Different Times



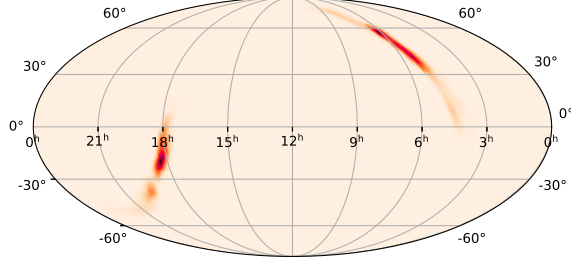
Sky location of the source viewed from the Earth at Different Times



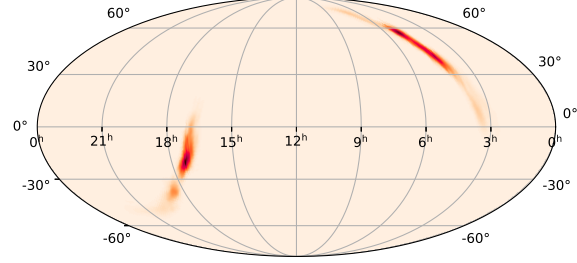
Sky location of the source viewed from the Earth at Different Times



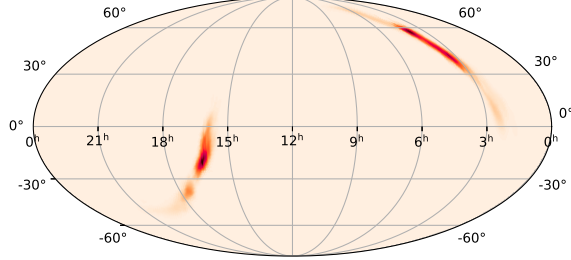
Sky location of the source viewed from the Earth at Different Times



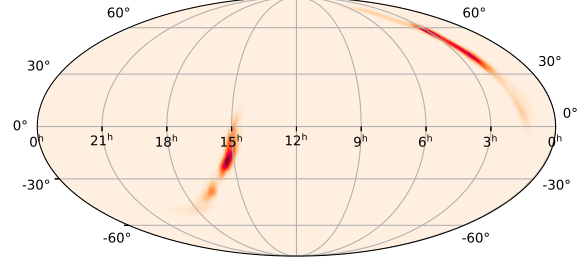
Sky location of the source viewed from the Earth at Different Times



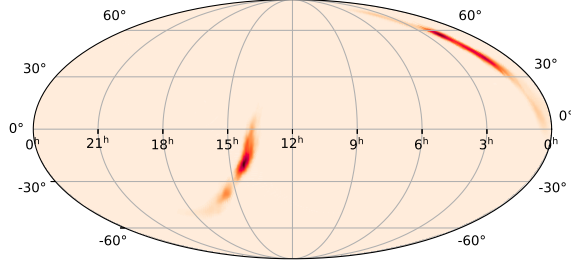
Sky location of the source viewed from the Earth at Different Times



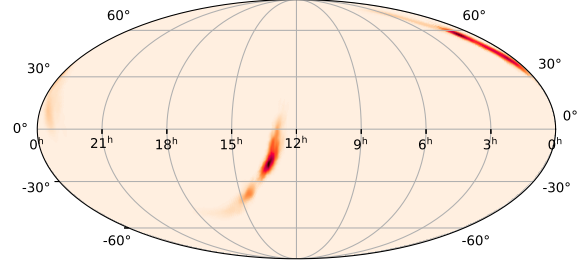
Sky location of the source viewed from the Earth at Different Times



Sky location of the source viewed from the Earth at Different Times



Sky location of the source viewed from the Earth at Different Times



B. Rotation of GW190519 PDF map in 24 hours (one map for each hour)

